The Astrophysical Journal, 803:30 (12pp), 2015 April 10 doi:10.1088/0004-637X/803/1/30

MAGNETIZATION DEGREE AT THE JET BASE OF M87 DERIVED FROM THE EVENT HORIZON TELESCOPE DATA: TESTING THE MAGNETICALLY DRIVEN JET PARADIGM

M. Kino[1,4], F. Takahara[2], K. Hada[3], K. Akiyama[3], H. Nagai[3], and B. W. Sohn[1]
[1] Korea Astronomy and Space Science Institute, 776 Daedeokdae-ro, Yuseong-gu, Daejeon 305-348, Korea; kino@kasi.re.kr
[2] Department of Earth and Space Science, Osaka University, Toyonaka 560-0043, Japan
[3] National Astronomical Observatory of Japan, 2-21-1 Osawa, Mitaka, Tokyo 181-8588, Japan
Received 2014 November 30; accepted 2015 February 10; published 2015 April 10

ABSTRACT

We explore the degree of magnetization at the jet base of M87 by using the observational data of the event horizon telescope (EHT) at 230 GHz obtained by Doeleman et al. By utilizing the method in Kino et al., we derive the energy densities of the magnetic fields (U_B) and electrons and positrons ($U_\pm$) in the compact region detected by EHT (the EHT region) with its FWHM size 40 μas. First, we assume that an optically thick region for synchrotron self-absorption (SSA) exists in the EHT region. Then, we find that the SSA-thick region should not be too large, in order to not overproduce the Poynting power at the EHT region. The allowed ranges of the angular size and the magnetic-field strength of the SSA-thick region are $21\,\mu\mathrm{as} \leqslant \theta_{\mathrm{thick}} \leqslant 26.3\,\mu\mathrm{as}$ and $50\,\mathrm{G} \leqslant B_{\mathrm{tot}} \leqslant 124\,\mathrm{G}$, respectively. Correspondingly, $U_B \gg U_\pm$ is realized in this case. We further examine the composition of plasma and energy density of protons by utilizing the Faraday rotation measurement at 230 GHz obtained by Kuo et al. Then, we find that $U_B \gg U_\pm + U_p$ still holds in the SSA-thick region. Second, we examine the case when the EHT region is fully SSA-thin. Then, we find that $U_B \gg U_\pm$ still holds unless protons are relativistic. Thus, we conclude that the magnetically driven jet scenario in M87 is viable in terms of energetics close to the Innermost Stable Circular Orbit scale unless the EHT region is fully SSA-thin and relativistic protons dominated.

Key words: galaxies: active – galaxies: jets – radio continuum: galaxies

1. INTRODUCTION

Elucidating the formation mechanism of relativistic jets in active galactic nuclei (AGNs) is one of the longstanding challenges in astrophysics. Although the magnetically driven jet and wind models are widely discussed in the literature (e.g., Okamoto 1974; Blandford & Znajek 1977; Blandford & Payne 1982; Chiueh et al. 1991; Li et al. 1992; Uchida 1997; Okamoto 1999; Koide et al. 2002; Tomimatsu & Takahashi 2003; Vlahakis & Konigl 2003; McKinney & Gammie 2004; Krolik et al. 2005; McKinney 2006; Komissarov et al. 2007, 2009; Tchekhovskoy et al. 2011; McKinney et al. 2013; Nakamura & Asada 2013; Toma & Takahara 2013), the actual value of the strength of the magnetic field (B) at the base of the jet is still an open problem. In order to test the magnetic jet paradigm, it is most essential to clarify the energy density of the magnetic fields ($U_B \equiv B_{\mathrm{tot}}^2/8\pi$) and that of the particles at the upstream end of the jet, where B_{tot} is the strength of the total magnetic fields.

Recently, short-millimeter radio observations at 1.3 mm (equivalent to the frequency 230 GHz) have been performed against the nearby giant radio galaxy, M87. M87 is located at a distance of $D_L = 16.7$ Mpc (Jordán et al. 2005; Blakeslee et al. 2009) and hosts one of the most massive supermassive black holes, $M_\bullet = (3-6) \times 10^9\,M_\odot$ (e.g., Macchetto et al. 1997; Gebhardt & Thomas 2009; Walsh et al. 2013), and thus M87 is known as the best target for studying the upstream end of the jet (e.g., Junor et al. 1999; Hada et al. 2011). The Schwarzschild radius is $R_s \equiv 2GM_\bullet/c^2 \approx 2 \times 10^{15}$ cm for the central black hole with $M_\bullet = 6 \times 10^9\,M_\odot$, where G is the gravitational constant and c is the speed of light. This corresponds to the angular size of $\sim 7\,\mu$as. Hereafter, we set this mass as the fiducial one. The Event Horizon Telescope (EHT), composed of stations in Hawaii and the western United States, has detected a compact region at the base of the M87 jet at 230 GHz with its size 40 μas (Doeleman et al. 2012). Furthermore, Kuo et al. (2014) obtained the first constraint on the Faraday rotation measure (RM) for M87, using the submillimeter array (SMA) at 230 GHz.

Short-millimeter VLBI observations of EHT at 230 GHz (equivalent to 1.3 mm) are crucially beneficial in order to minimize the blending effect of substructures below the spatial resolutions of telescopes. Historically, single-dish observations of AGN jets at the centimeter waveband (with arcminutes spatial resolution) revealed that their spectra are flat at the centimeter waveband (Owen et al. 1978). Marscher (1977) suggested the importance of VLBI observations for distinguishing various possible explanations for the observed flatness. Cotton et al. (1980) conducted VLBI observations at the centimeter waveband and found that the flat spectrum results from a blending effect of substructures with the milliarcsecond (μas) scale. This was a significant forward step. However, subsequent VLBI observations have revealed that such μas-scale components still have substructures when observed at higher spatial resolution (i.e., shorter wavelength). This is a vicious circle between telescopes' spatial resolutions and the sizes of the substructures. In the case of M87, we finally start to overcome this problem because the spatial resolution of EHT almost reaches one of the fundamental scales, i.e., the Innermost Stable Circular Orbit (ISCO) scale (Doeleman et al. 2012). Hence, in this work, we will assume the ISCO radius (R_{ISCO}) to be the minimum size of the jet nozzle.

Motivated by the significant observational progresses by EHT, we explore the magnetization degree ($U_\pm/U_B$) in the core of M87 seen at 230 GHz. We note that Doeleman et al. (2012)

[4] Last update: XX, 2014.

did not derive $B_{\rm tot}$ and $U_\pm/U_B$, and we will estimate them at the EHT region for the first time. In the theoretical point of view, we have developed the methodology for the estimation of $U_\pm/U_B$ and $B_{\rm tot}$ in Kino et al. (2014; hereafter K14), and it is also applicable to 230 GHz. In K14, we estimated $U_\pm/U_B$ and $B_{\rm tot}$ in the radio core at 43 GHz with $\theta_{\rm FWHM} = 110\,\mu$as and 0.7 Jy. We obtained the tight constraint of field strength ($1\,{\rm G} \leqslant B_{\rm tot} \leqslant 15\,{\rm G}$), but the resultant energetics are consistent with either the $U_\pm$-dominated or U_B-dominated ($1 \times 10^{-5} \leqslant U_\pm/U_B \leqslant 6 \times 10^2$) cases. The radio core at 230 GHz with $\theta_{\rm FWHM} = 40\,\mu$as directly corresponds to the upstream end of the M87 jet and would then give the tightest constraints for testing the magnetic jet paradigm. The goal of this work is applying the method of K14 to the EHT-detected region and exploring its properties.

Opacity of the EHT region against synchrotron self-absorption (SSA) is critically important. We should emphasize that it is not clear whether the EHT region is SSA-thick or not because short-millimeter VLBI observations are conducted only at 230 GHz, and therefore it is not possible to obtain spectral information at the moment. Intriguingly, Rioja & Dodson (2011) detect the core-shift between 43 and 86 GHz (in Figure 5 in their paper), which means that the radio core at 86 GHz contains the SSA-thick region. With the aid of interferometry observations, we can also infer the turnover frequency. The fluxes measured by IRAM at 89 GHz (Despringre et al. 1996) and by SMA at 230 GHz (Tan et al. 2008) also seem to indicate that the radio core is SSA-thick above 89 GHz, although the data are not obtained simultaneously (see also Abdo et al. 2009). The submillimeter spectrum obtained by ALMA also shows the spectral break above ~100 GHz (Doi et al. 2013). Therefore, we may infer that the SSA turnover frequency for the EHT region is above ~100 GHz. As a working hypothesis, we first assume that the EHT region includes the SSA-thick region and apply the method of K14. We will also discuss the fully SSA-thin case in Section 6.

The layout of this paper is as follows. In Section 2, we briefly review the method of K14. In Section 3, we apply the method to the EHT region. In Section 4, the resultant $U_\pm/U_B$ and $B_{\rm tot}$ are presented. In Section 5, we further discuss constraints on the proton component. In Section 6, we discuss the fully SSA-thin case. In Section 7, we summarize the results and give an account of important future work to be pursued. In this work, we define the radio spectral index α as $S_\nu \propto \nu^{-\alpha}$.

2. METHOD

Following K14, here we briefly review the method for constraining the magnetic field and relativistic electrons in radio cores.

2.1. Basic Assumptions

First of all, we show the main assumptions in this work.

1. We assume that the emission region is spherical with its radius R ,which is defined as $2R = \theta_{\rm obs} D_A$, where $\theta_{\rm obs}$, $D_A = D_L/(1+z)^2$, and D_L are the observed angular diameter of the emission region, the angular diameter distance, and the luminosity distance, respectively. This is justified by the following observational suggestion. In the EHT observation of M87 in 2012, Akiyama et al. (2015) measured the closure phase of M87 among the three stations (SMA, CARMA, and SMT). The closure phase is the sum of the visibility phases on a triangle of three stations (e.g., Thompson et al. 2001; Lu et al. 2012). Akiyama et al. (2015) showed that the measured closure phases are close to zero ($\lesssim \pm 20^\circ$) for the structure detected in Doeleman et al. (2012), which is naturally explained by a symmetric emission region and disfavors a significantly asymmetric one.
2. We do not include the general reletavistic (GR) effect for simplicity. The full GR ray-tracing and radiative transfer may be essential for reproducing the detailed shape of the black hole shadows (e.g., Falcke et al. 2000; Takahashi 2004; Broderick & Loeb 2009; Nagakura & Takahashi 2010; Dexter et al. 2012; Lu et al. 2014). However, current EHT can only detect flux from a bright region via the visibility amplitude, and the spatial structure can be constrained only by closure phases (e.g., Doeleman et al. 2009). Although the predicted black hole shadow images in detail seem diverse, the size of the bright region is roughly comparable to the ISCO scale (e.g., Fish et al. 2013 for review). Therefore, we do not include the GR effect, but explore a fairly wide allowed range for the bright region size, $\theta_{\rm thick}$, i.e., from $\sim R_{\rm ISCO}$ to $\sim 2R_{\rm ISCO}$ (see Section 5).

2.2. General Consideration

Given the SSA turnover frequency ($\nu_{\rm ssa}$) and the angular diameter size of the emission region at $\nu_{\rm ssa}$, one can uniquely determine $B_{\rm tot}$ and $K_\pm$, where $K_\pm$ is the normalization factor of relativistic (nonthermal) electrons and positrons (e.g., Kellermann & Pauliny-Toth 1969; Burbidge et al. 1974; Jones et al. 1974a, 1974b; Blandford & Rees 1978; Marscher 1987). Recently, K14 points out that the observing frequency is identical to $\nu_{\rm ssa}$ when we can identify the SSA-thick surface at the observing frequency.

As a first step, we assume that the EHT region is a one-zone sphere with isotropic magnetic field ($B_{\rm tot}$) and particle distributions in the present work. Locally, we denote ($B_{\perp,{\rm local}} = B_{\rm tot} \sin\alpha$) as the magnetic-field strength perpendicular to the direction of electron motion (Ginzburg & Syrovatskii 1965 hereafter GS65), where α is the pitch angle between the vectors of electron velocity and the magnetic field (e.g., Rybicki & Lightman 1979). Then, we can obtain pitch-angle-averaged $B_{\perp,{\rm local}}$, defined as $B_\perp$, as follows:

$$B_{\rm tot}^2 = \frac{3}{2} B_\perp^2 \tag{1}$$

because $B_\perp^2 = (1/4\pi)\int B_{\rm tot}^2 \sin^2\alpha d\Omega = 2B_{\rm tot}^2/3$. (This is a slightly different definition of $B_\perp$ than given in K14. The corresponding slight changes of numerical factors are summarized in the Appendix.) Because we assume an isotropic field, hereafter we choose the $B_\perp$ direction to the line of sight (LOS).

The number density distribution of relativistic electrons and positrons $n_\pm(\epsilon_\pm)$ is defined as (e.g., Equation (3.26) in GS65)

$$n_\pm(\epsilon_\pm) d\epsilon_\pm = K_\pm \epsilon_\pm^{-p} d\epsilon_\pm \quad (\epsilon_{\pm,\min} \leqslant \epsilon_\pm \leqslant \epsilon_{\pm,\max}), \tag{2}$$

where $\epsilon_\pm = \gamma_\pm m_e c^2$, $p = 2\alpha + 1$, $\epsilon_{\pm,\min} = \gamma_{\pm,\min} m_e c^2$, and $\epsilon_{\pm,\max} = \gamma_{\pm,\max} m_e c^2$ are the electron energy, spectral index, minimum energy, and maximum energy of relativistic

(nonthermal) electrons and positrons, respectively. Although electrons and positrons may have a different heating/acceleration process in $e^-/e^+/p$ mixed plasma (e.g., Hoshino & Arons 1991), here we assume that minimum energies of electrons and positrons are the same for simplicity. By evaluating the emission at the SSA frequency, we obtain

$$B_\perp = b(p)\left(\frac{\nu_{\rm ssa,obs}}{1\ {\rm GHz}}\right)^5\left(\frac{\theta_{\rm obs}}{1\ {\rm mas}}\right)^4\left(\frac{S_{\nu_{\rm ssa},\rm obs}}{1\ {\rm Jy}}\right)^{-2} \times\left(\frac{\delta}{1+z}\right), \quad (3)$$

where $b(p)$ is tabulated in Marscher (1983), Hirotani (2005), and K14. The term $K_\pm$ is given by

$$K_\pm = k(p)\left(\frac{D_{\rm A}}{1\ {\rm Gpc}}\right)^{-1}\left(\frac{\nu_{\rm ssa,obs}}{1\ {\rm GHz}}\right)^{-2p-3}\left(\frac{\theta_{\rm obs}}{1\ {\rm mas}}\right)^{-2p-5} \times\left(\frac{S_{\nu_{\rm ssa},\rm obs}}{1\ {\rm Jy}}\right)^{p+2}\left(\frac{\delta}{1+z}\right)^{-p-3}, \quad (4)$$

where $k(p)$ is tabulated in K14. The cgs units of $K_\pm$ and $k(p)$ depend on p: erg $^{p-1}$ cm^{-3}. It is useful to show the explicit expression of the ratio $U_\pm/U_B$ as follows:

$$\frac{U_\pm}{U_B} = \frac{16\pi}{3b^2(p)}\frac{k(p)\epsilon_{\pm,\rm min}^{-p+2}}{(p-2)}\left(\frac{D_{\rm A}}{1\ {\rm Gpc}}\right)^{-1}\left(\frac{\nu_{\rm ssa,obs}}{1\ {\rm GHz}}\right)^{-2p-13} \times\left(\frac{\theta_{\rm obs}}{1\ {\rm mas}}\right)^{-2p-13}\left(\frac{S_{\nu_{\rm ssa},\rm obs}}{1\ {\rm Jy}}\right)^{p+6}\left(\frac{\delta}{1+z}\right)^{-p-5} \quad ({\rm for}\quad p>2). \quad (5)$$

From this, we find that $\nu_{\rm ssa,obs}$ and $\theta_{\rm obs}$ have the same dependence on p. Using this relation, we can estimate $U_\pm/U_B$ without the minimum energy (equipartition B field) assumption. It is clear that the measurement of $\theta_{\rm obs}$ is crucial for determining $U_\pm/U_B$.

We further impose two general constraint conditions.

1. Time-averaged total power of the jet ($L_{\rm jet}$) estimated by jet dynamics at large scale should not be exceeded by the one at the jet base

$$L_{\rm jet} \geqslant \max\left[L_{\rm poy}, L_\pm\right],$$
$$L_\pm = \frac{4\pi}{3}\Gamma^2\beta R^2 c U_\pm,$$
$$L_{\rm poy} = \frac{4\pi}{3}\Gamma^2\beta R^2 c U_B, \quad (6)$$

where $L_\pm$, $L_{\rm poy}$, Γ, and βc are electron/positron kinetic power, Poynting power, bulk Lorentz factor, and bulk speed of the jet at the EHT region, respectively. Note that U_B, $U_\pm$, and R are directly constrained by the VLBI observations.

2. The minimum Lorentz factor of the relativistic electrons and positrons ($\gamma_{\pm,\rm min}$) should be smaller than the ones radiating the observed synchrotron emission ($\nu_{\rm syn,obs}$); for example, 230 GHz. Otherwise, we would not be able to observe the synchrotron emission at the corresponding frequency. This is generally given by

$$\nu_{\rm syn,obs} \geqslant 1.2\times10^6 B_\perp \gamma_{\pm,\rm min}^2\frac{\delta}{1+z}. \quad (7)$$

These relations significantly constrain the allowed values of $\gamma_{\pm,\rm min}$ and $B_{\rm tot}$.

In the next section, we will add another constraint condition (i.e., minimum size limit).

3. APPLICATION TO THE EHT REGION

Here we apply the method to the EHT region in M87.

3.1. On the Basic Physical Quantities

Here we list the basic physical quantities of the M87 jet.

1. The total jet power, $L_{\rm jet}$, can be estimated by considering jet dynamics at well-studied bright knots (such as knots A, D, and *Hubble Space Telescope*-1) located at the kiloparsec scale (e.g., Bicknell & Begelman 1996; Owen et al. 2000; Stawarz et al. 2006). Based on the literature on these studies, here we adopt

$$1\times10^{44}\ {\rm erg\ s^{-1}} \leqslant L_{\rm jet} \leqslant 5\times10^{44}\ {\rm erg\ s^{-1}}, \quad (8)$$

(see also Rieger & Aharonian 2012 for review). We note that Young et al. (2002) indicate $L_{\rm jet}\sim3\times10^{42}$ erg s^{-1} based on the X-ray bubble structure, which is significantly smaller than the aforementioned estimate. The smallness of $L_{\rm jet}$ estimated by Young et al. (2002) could be attributed to a combination of intermittency of the jet and an averaging of $L_{\rm jet}$ on a long timescale of the X-ray cavity age. In this work, we do not utilize this small $L_{\rm jet}$.

2. We would assume that the bulk speed of the jet is in a nonrelativistic regime at the jet at the EHT region because both theory and observations currently tend to indicate slow and gradual acceleration, so that the flow reaches the relativistic speed around $10^{3-4}\,R_s$ (McKinney 2006; Asada et al. 2014; Hada et al. 2014). The brightness temperature of the 230 GHz radio core is below the critical temperature $\sim10^{11}$ K limited by the inverse-Compton catastrophe process (Kellermann & Pauliny-Toth 1969). When the 230 GHz emission originates from the SSA-thick plasma, the characteristic electron temperature is comparable to T_b (e.g., Loeb & Waxman 2007), and T_b at 230 GHz is in a relativistic regime. Therefore, we set

$$\Gamma\beta = c_{\rm sound} = \frac{1}{\sqrt{3}}, \quad (9)$$

where $c_{\rm sound}$ is the sound speed of relativistic matter. This will be used in Equation (6) as $\Gamma^2\beta = 1/\sqrt{3}$.

3. Last, we summarize three differences between this work and Doeleman et al. (2012) in terms of the assumptions on basic physical quantities. In this work, we attempt to reduce assumptions and treat the EHT region in a more general way. (1) Doeleman et al. (2012) assume that the EHT region size is identical to the ISCO size itself, which reflects the degree of the black hole spin. In this work, we

do not use this assumption. (2) Doeleman et al. (2012) seem to focus on the SSA-thin case. In this work, we will investigate both the SSA-thick and SSA-thin cases. (3) Doeleman et al. (2012) seem to assume $\theta_{\rm FWHM}$ as the physical size of the EHT region. In this work, we take into account a deviation factor between $\theta_{\rm FWHM}$ and its physical size (e.g., Marscher 1983).

3.2. Difficulties for the SSA-thick One-zone Model

First, we estimate the magnetic-field strength in the EHT region by assuming that all of the EHT region with $\theta_{\rm FWHM} = 40\,\mu$as is fully SSA-thick. The field strength of the EHT region is estimated as

$$B_{\rm tot} = 3.4 \times 10^2\,{\rm G}\left(\frac{\nu_{\rm ssa,obs}}{230\,{\rm GHz}}\right)^5 \times \left(\frac{\theta_{\rm obs}}{72\,\mu{\rm as}}\right)^4\left(\frac{S_{\nu_{\rm ssa},{\rm obs}}}{1.0\,{\rm Jy}}\right)^{-2}\left(\frac{\delta}{1+z}\right). \quad (10)$$

Marscher (1983) pointed out VLBI-measured $\theta_{\rm FWHM}$ is connected with true angular size $\theta_{\rm obs}$ by the relation $\theta_{\rm obs} \approx 1.8\theta_{\rm FWHM}$ for partially resolved sources (see also Krichbaum et al. 2006; Loeb & Waxman 2007). Taking such deviation into account, we examine the case of $72\,\mu{\rm as} = 1.8 \times 40\,\mu$as for the estimate of B-field strength.

What happens with this field strength?

3.2.1. Too-large Poynting Power

A severe problem arises if $B_{\rm tot} \approx 3 \times 10^2$ G is realized. Because we assume a nearly isotropic random field, which can be supported by the low linear polarization degree at 230 Ghz (Kuo et al. 2014), the corresponding Poynting power is given by

$$L_{\rm poy} = 1.5 \times 10^{47}\,{\rm erg\,s^{-1}} \times \left(\frac{B_{\rm tot}}{300\,{\rm G}}\right)^2\left(\frac{2R}{1.8\times10^{16}\,{\rm cm}}\right)^2. \quad (11)$$

Here we adopt $2R = 1.8 \times 10^{16}\,{\rm cm} = 1.8 \times 40\,\mu as \times 16.7\,{\rm Mpc}$. When the total power of the jet (i.e., the sum of the kinetic and Poynting ones) is conserved along the jet at a large scale, then this is too large compared with the jet's mean kinetic power inferred from its large-scale dynamics of a few $\times 10^{44}$ erg s^{-1} (e.g., Rieger & Aharonian 2012 for review) We emphasize that a constraint on $B_{\rm tot}$ by $L_{\rm poy}$ is almost model-independent.

If we allow some kind of fast magnetic reconnection processes (e.g., Kirk & Skjæraasen 2003; Bessho & Bhattacharjee 2007; Bessho & Bhattacharjee 2012; Takamoto et al. 2012), in order to dissipate the magnetic fields at the EHT region, then fast and large variabilities would be naturally expected. However, there is no observational support for such variabilities. Therefore, it seems difficult to realize too-large $B_{\rm tot}$ at the EHT region.

3.2.2. Too-fast Synchrotron Cooling

Once we obtain a typical value of $B_{\rm tot}$, then we can estimate a typical synchrotron-cooling timescale. It significantly characterizes the observational behavior of the EHT region. The synchrotron-cooling timescale is correspondingly

$$t_{\pm,{\rm syn}} \approx 1 \times 10^{-2}\,{\rm day}\left(\frac{B_{\rm tot}}{300\,{\rm G}}\right)^{-2}\left(\frac{\gamma_\pm}{10}\right)^{-1}. \quad (12)$$

This is much shorter than the day scale, although the flux at 230 GHz measured by the EHT remains constant during the subsequent 3 days (see the Supplementary Material of Doeleman et al. 2012). Then, a difficulty arises due to this short $t_{\pm,{\rm syn}}$. The 230 GHz radio-emitting electrons are in the so-called fast cooling regime (Sari et al. 1998) in which injected electrons instantaneously cool down by synchrotron cooling. Hence, a slight change/fluctuation of B-field strength instantaneously (on timescale $t_{\pm,{\rm syn}}$) is reflected on the synchrotron flux at the EHT region. Hence, for realizing the observed constant flux, a constant plasma supply of $B_{\rm tot}$ and $K_\pm$ with very small fluctuation is required to avoid rapid variability/decrease of the synchrotron flux. On the other hand, when the magnetic fields are not that large, $t_{\pm,{\rm syn}}$ can become longer than the day scale. Then, we can avoid the rapid variability/decrease of the synchrotron flux without imposing a very small fluctuation of $B_{\rm tot}$ and $K_\pm$ in the bulk flow. Because some fine-tuning of the $B_{\rm tot}$ and $K_\pm$ injection may be able to adjust the observed constant flux density at the EHT region, the too-fast cooling problem may be less severe than the aforementioned problem on too-large $L_{\rm poy}$. However, it is natural to suppose that smaller $B_{\rm tot}$ realizes in the EHT region to avoid fine-tuning of injection quantities.

3.3. Two-zone Model

3.3.1. Basic Idea

The difficulty of too-large $L_{\rm poy}$ can be resolved if the EHT region is composed of SSA-thick and SSA-thin regions, and the angular size of the SSA-thick region ($\theta_{\rm thick}$) is more compact than $\theta_{\rm obs}$, i.e.,

$$\theta_{\rm obs} > \theta_{\rm thick}. \quad (13)$$

We show an illustration of our scenario in Figure 1. In this solution, most of the correlated flux density detected by EHT is attributed to the emission from the SSA-thin region. Because the $\nu_{\rm ssa}$ of the SSA-thin region is by definition smaller than 230 GHz, the magnetic field must be significantly smaller because the field strength is proportional to $\nu_{\rm ssa}^5$. For of this reason, we regard the SSA-thick region as the main carrier of the Poynting power.

Here, we assume the ISCO radius for a nonrotating black hole ($R_{\rm ISCO} = 6GM_\bullet/c^2 = 3R_s \equiv \theta_{\rm ISCO}D_L$) as the minimum size of the SSA-thick region. This corresponds to the angular size, 21 μas. Indeed, theoretical works (Broderick & Loeb 2009; Lu et al. 2014) comparing the EHT observations and jet models also indicate model images with short-millimeter bright region,[5] with their size comparable to ISCO. Therefore, we examine the range of the SSA-thick region, $\theta_{\rm thick} \geqslant 21\,\mu$as.

[5] Conventionally, such regions are sometimes called hotspots in the literature (e.g., Lu et al. 2014 and reference therein).

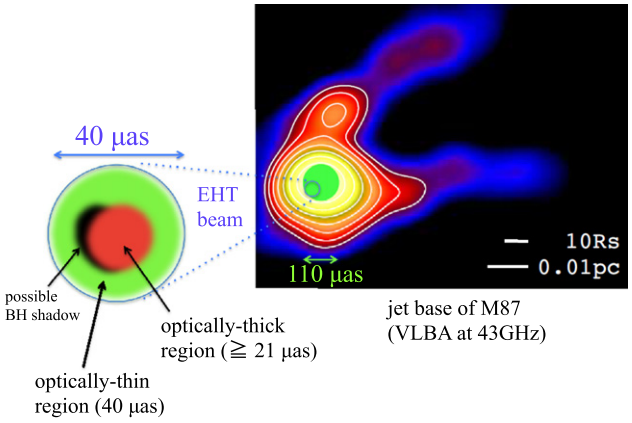

Figure 1. Illustration of the jet base of M87 down to the EHT region scale. The right panel shows the actual image of M87 with VLBA at 43 GHz adopted from Hada et al. (2013). The yellow–green circle shows the one-zone region with its diameter, 110 μas, which is investigated in K14. The EHT region detected by Doeleman et al. (2012) is shown as the blue circle. Because Hada et al. (2011) indicate that the central engine of M87 is located at ~41 μas eastward of the radio core at 43 GHz, we put the EHT region around there. The left panel shows the illustration of the internal structure inside the EHT region. The red-colored region represents an SSA-thick compact region inside the SSA-thin region. The black-colored region conceptually shows a possible BH shadow image. According to the smallness of the closure phase reported in Akiyama et al. (2015), a certain level of symmetry is kept in this picture.

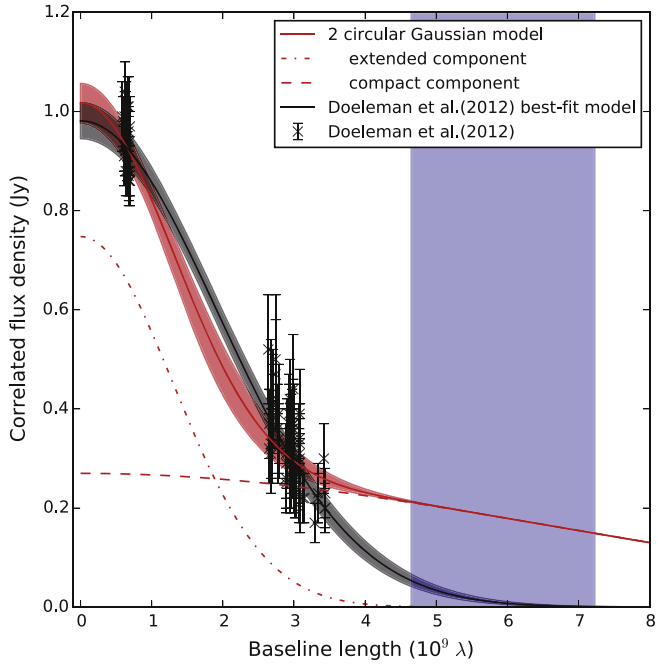

Figure 2. Gaussian fittings to the correlated flux density of the M87 core obtained by EHT at 230 GHz. The flux density data, plotted as a function of baseline length, are adopted from Doeleman et al. (2012). The black solid curve is the best-fit circular Gaussian model with $S_\nu = 0.98$ Jy and $\theta_{\rm FWHM} = 40$ μas obtained by Doeleman et al. (2012). The red solid curve is the best-fit two-component model. The red dashed and dot-dashed curves represent the SSA-thick and the SSA-thin components, respectively. The SSA-thick component is expressed as the Gaussian with $\theta_{\rm FWHM} = 21$ μas/1.8 = 11.1 μas and $S_\nu = 0.27$ Jy. The size and the flux density of the extended SSA-thin component are $\theta_{\rm FWHM} = 60$ μas and $S_\nu = 0.75$ Jy. The blue-shaded region represents the range which contains the baseline length between the Hawaii/Arizona/California and Chile stations.

3.3.2. Gaussian Fitting with Two Components

In Figure 2, we estimate the correlated flux density of this SSA-thick region based on the EHT data. The observed flux data, plotted as a function of baseline length, are adopted from Doeleman et al. (2012). The black solid curve is the best-fit circular Gaussian model by Doeleman et al. (2012). The red solid curve is the best-fit model. The red dashed and dot-dashed curves represent the SSA-thick and the SSA-thin components, respectively.

Below, we explain the details of the Gaussian fitting. To determine the correlated flux density for the compact SSA-thick region with its lower limit size, $\theta_{\rm FWHM} = 21$ μas/1.8 = 11.1 μas, we conduct the two-component (SSA-thick and thin components) Gaussian fitting to the EHT data. First, we obtain the upper limit of the correlated flux density for the SSA-thick component as $S_\nu = 0.27$ Jy. Next, we perform the the two-component (SSA-thick and thin components) Gaussian fitting by fixing $\theta_{\rm FWHM} = 21$ μas/1.8 = 11.1 μas and $S_\nu = 0.27$ Jy. Then, we obtain the corresponding size and flux of the extended SSA-thin component, $S_\nu = 0.75$ Jy and $\theta_{\rm FWHM} = 60$ μas.

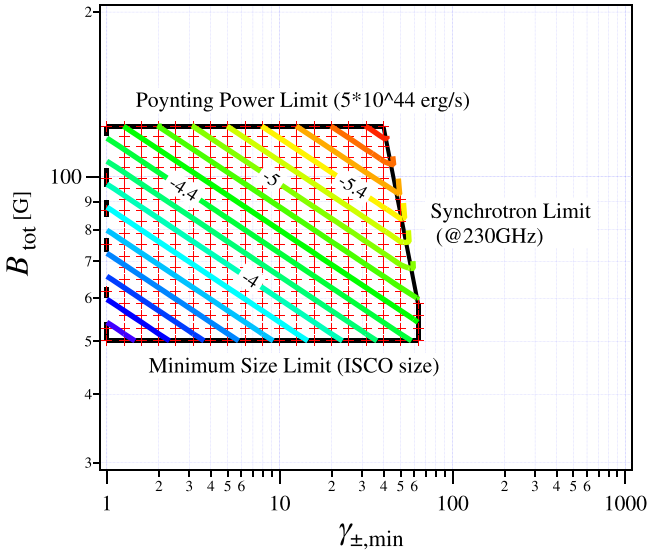

Figure 3. Allowed region of $\gamma_{\pm,\rm min}$ and $B_{\rm tot}$ (the red cross points enclosed by the black trapezoid). The colored contour lines show the allowed log $(U_\pm/U_B)$. The tags log $(U_\pm/U_B) = -4$, −4.4, −5, and −5.4 are marked as reference values. The physical quantities and parameters adopted are $L_{\rm jet} = 5 \times 10^{44}$ erg s^{-1} and $p = 3.0$. The minimum $\gamma_\pm$ is limited by $\nu_{\rm syn,obs}$ at 230 GHz.

4. RESULTS

Here, we limit on $B_{\rm tot}$, $\theta_{\rm thick}$, and $U_\pm/U_B$, in the EHT region without assuming plasma composition. The critical value, $\gamma_{\pm,\rm min}$, is derived by the combination of the jet power limit (Equation (6)) and the synchrotron emission limit (Equation (7)). By eliminating $B_{\rm tot}$, we obtain

$$\gamma_{\pm,\rm min} \leqslant 1.2 \times 10^2 \times \left(\frac{2R}{1.8 \times 10^{16}\ {\rm cm}}\right)^{1/2} \left(\frac{L_{\rm jet}}{5 \times 10^{44}\ {\rm erg\ s^{-1}}}\right)^{-1/4}, \quad (14)$$

where $\nu_{\rm ssa} = 230$ GHz is used. Because $\gamma_{\pm,\rm min}$ has R dependence, larger R allows slightly larger $\gamma_{\pm,\rm min}$.

In Figure 3, we show the value of log $(U_\pm/U_B)$ in the allowed ranges of $\gamma_{\pm,\rm min}$ and $B_{\rm tot}$ with $L_{\rm jet} = 5 \times 10^{44}$ erg s^{-1} and $p = 3.0$. It is essential to note that the maximum value of $B_{\rm tot}$ is determined by the condition $L_{\rm poy} \leqslant L_{\rm jet}$ whereas the

Table 1
Results When the EHT Region Contains the SSA-thick Region

L_j (erg s^{-1})	Allowed $B_{\rm tot}$ (G)	Allowed $\theta_{\rm thick}$ (μas)	Allowed $U_\pm/U_B$
5×10^{44}	$50 \leqslant B_{\rm tot} \leqslant 124$	$21 \leqslant \theta_{\rm thick} \leqslant 26.3$	$7.9\times10^{-7} \leqslant \frac{U_\pm}{U_B} \leqslant 2.3\times10^{-3}$

minimum value of $B_{\rm tot}$ is governed by the condition of $\theta_{\rm thick} \geqslant R_{\rm ISCO}/D_L \approx 21\,\mu$as. The right side of the allowed region is determined by the $\nu_{\rm syn,obs}$ limit shown in Equation (7). Note that the maximum value of $\theta_{\rm thick} = 26.3\,\mu$as is smaller than 40 μas. This suggests that the EHT region has a more compact SSA-thick component in it. Interestingly, overall the SSA-thick region satisfies $U_B \gg U_\pm$. If protons do not contribute to jet energetics, then this result supports the magnetically driven jet scenario. In Table 1 we show the resultant allowed values. Summing up, we find that (1) the allowed $\theta_{\rm thick}$ satisfies $21\,\mu{\rm as} \leqslant \theta_{\rm thick} \leqslant 26.3\,\mu$as and that (2) the allowed field strength is $50\,{\rm G} \leqslant B_{\rm tot} \leqslant 124\,{\rm G}$.

When we choose a smaller L_j, the upper limit of $\theta_{\rm thick}$ and $B_{\rm tot}$ becomes smaller, according to Equations (3) and (6). When $L_j = 1\times10^{44}\,{\rm erg\,s^{-1}}$, the allowed $B_{\rm tot}$ and $\theta_{\rm thick}$ are $50\,{\rm G} \leqslant B_{\rm tot} \leqslant 65\,{\rm G}$ and $21\,\mu{\rm as} \leqslant \theta_{\rm thick} \leqslant 22.4\,\mu$as. In this case, the allowed regions of $B_{\rm tot}$ and $\theta_{\rm thick}$ are very narrow.

We add a short comment on the brightness temperature. The brightness temperature of the SSA-thick region can be estimated as

$$T_b = \frac{S_{\nu,\rm obs}c^2}{2\pi k\nu_{\rm syn,obs}^2\left(\theta_{\rm thick}/2\right)^2} \approx 2\times10^{10}\,K\left(\frac{S_{\nu,\rm obs}}{0.27\,{\rm Jy}}\right)\left(\frac{\theta_{\rm thick}}{21\,\mu{\rm as}}\right)^{-2}, \quad (15)$$

where $\nu_{\rm syn,obs} = 230\,{\rm GHz}$. This value is comparable with the T_b at 86 GHz estimated by Lee (2013).

Last, it is worthwhile to add the following. According to the equation of state in the relativistic temperature regime (e.g., Chandrasekhar 1967; Kato et al. 1998), we obtain[6]

$$\gamma_{\pm,\rm ssa} \approx 3\frac{kT_b}{m_ec^2} \approx 10\left(\frac{\theta_{\rm thick}}{21\,\mu{\rm as}}\right)^{-2}, \quad (16)$$

where we use the fact that $\gamma_{\pm,\rm min}m_ec^2$ can be identical to the average energy of the electrons and positrons because p is steeper than 2. The obtained $\gamma_{\pm,\rm ssa}$ tends to be smaller than the minimum Lorentz factor obtained by Equation (14) by a factor of a few. While we may use $\gamma_{\pm,\rm ssa}$ as $\gamma_{\pm,\rm min}$, we conservatively use the condition Equation (14), taking some uncertainty of a numerical factor in Equation (14) into account.

[6] When magnetic fields are uniform, the numerical factor at the right-hand side in Equation (16) is smaller than this case because of fewer degrees of freedom for the electrons/positrons (see Slysh 1992; Tsang & Kirk 2007).

5. CONSTRAINTS ON THE PROTON COMPONENT

In Section 5, we investigate constraint on the energy density of protons (U_p) by using Faraday RM measured by Kuo et al. (2014). From the measured RM, we will constrain the number density of the protons (n_p). Then, we examine U_p. The degree of proton contribution in the energetics has a significant influence over the relativistic jet formation (e.g., Begelman et al. 1984; Reynolds et al. 1996).

5.1. Further Assumptions

To discuss the proton contribution, we need to add some further assumptions. Although the observed radio emissions warrant the existence of the relativistic e^-/e^+ population, the origin of relativistic e^-/e^+, which radiate radio emissions at 230 GHz, is not clear. There are several possibilities for its origin. Relativistic protons may play an important role for heating/acceleration of positrons via a resonance process with relativistic protons in shocked regions (e.g., Hoshino & Arons 1991), whereas direct $e^\pm$ pair injection (Iwamoto & Takahara 2002; Asano & Takahara 2009) and/or relativistic neutron injection (Toma & Takahara 2012) processes may also work at the jet formation regions. It is beyond the scope of this work to clarify the origin of the relativistic e^-/e^+ population and their relation with the proton component. In this section, we simply assume the existence of protons and generally define the average energy of these protons as ϵ_p.

As mentioned in the Introduction, Kuo et al. (2014) obtained the first constraint on RM for M87 using SMA at 230 GHz. Although it is not clear how much a fraction of linearly polarized emission comes from the EHT region, it is worthwhile to extend the method used in the previous sections by including the RM constraint and applying it to the present case of the 230 GHz core of M87. The degree of LP ~1% at 230 GHz detected by Kuo et al. (2014) is significantly smaller than the degree of LP when magnetic fields are fully ordered (i.e., typically ~70% for the SSA-thin case and ~16% for the SSA-thick case; see Pacholczyk 1970). Hence, the assumption of isotropic B-fields in this work looks reasonable to some extent. On the other hand, only ordered magnetic fields aligned to the LOS ($B_{\rm LOS}$) contribute to the RM. Hereafter, we conservatively assume $B_{\rm tot} \geqslant B_{\rm LOS}$.

5.2. RM Limit

Here we introduce a new constraint using the RM observation data. This RM is important for estimating the kinetic power of the protons (L_p) because RM can constrain the proton number density. Generally speaking, an observed rotation measure ($\rm RM_{obs}$) consists of two parts, i.e., RM by internal (jet) ($\rm RM_{jet}$) and RM by external (foreground) matter ($\rm RM_{ext}$). Therefore, the $\rm RM_{obs}$ can be decomposed into

$$\rm RM_{obs} = RM_{jet} + RM_{ext}. \quad (17)$$

Basically, it is difficult to decouple $\rm RM_{jet}$ and $\rm RM_{ext}$ and obtain $\rm RM_{jet}$. However, it may be possible to discuss an upper limit of $|\rm RM_{jet}|$ with some reasonable assumptions. When the observed RM ($\rm RM_{obs}$) is comparable to $\rm RM_{ext}$, then we obtain

$$\rm RM_{obs} \approx RM_{ext}, \quad \left|RM_{jet}\right| \ll RM_{obs}. \quad (18)$$

Indeed, the foreground Faraday screen in close vicinity of the jets seems to well explain the observed $\mathrm{RM_{obs}}$ for radio-loud AGNs (e.g., Zavala & Taylor 2004). The explicit form of $\mathrm{RM_{jet}}$, the rotation measure for relativistic plasma, is given as

$$\begin{aligned}\left|\mathrm{RM_{jet}}\right| &= \frac{e^3}{2\pi m_e^2 c^4}\int dl B_{\mathrm{LOS}} n_p \frac{\log\gamma_{\pm,\mathrm{min}}}{2\gamma_{\pm,\mathrm{min}}^2} \\ &\leqslant 5.36\times 10^3 B_{\mathrm{tot}} n_p \frac{\log\gamma_{\pm,\mathrm{min}}}{2\gamma_{\pm,\mathrm{min}}^2} \\ &\times\left(\frac{R}{10^{16}\,\mathrm{cm}}\right)\mathrm{rad\,m^{-2}}, \end{aligned} \tag{19}$$

where we set $\int dl \approx 2R$ because the region is assumed as uniform. From this, we see that Faraday rotation is strongly suppressed in relativistic plasma (Jones & Odell 1977; Quataert & Gruzinov 2000; Broderick & McKinney 2010). Note that RM only includes the ionic plasma contribution and does not include the electron/positron-pair plasma. This is because the electron and positron have the same mass but have opposite (i.e., minus and plus) charges, and then the net Faraday rotation by them is canceled out. Qualitatively saying, the mixture of the $e^{\pm}$-pair plasma (i.e., $\eta < 1$) effectively reduces the value of $\mathrm{RM_{jet}}$.

Regarding the RM limit of M87, Kuo et al. (2014) have measured $|\mathrm{RM_{obs}}| \approx (3.4-7.5)\times 10^5\,\mathrm{rad\,m^{-2}}$, and they assume $\mathrm{RM_{obs}} \approx \mathrm{RM_{ext}}$. Following Kuo et al. (2014), we also assume $\mathrm{RM_{obs}} \approx \mathrm{RM_{ext}}$. Then, the RM limit can be written as

$$\left|\mathrm{RM_{jet}}\right| \leqslant 1\times 10^5\,\mathrm{rad\,m^{-2}}. \tag{20}$$

Note that the above constraint only gives the upper limit of n_p. Therefore, the finite value of $|\mathrm{RM_{jet}}|$ does not exclude the plasma composition of pure $e^{\pm}$ plasma.

In Section 5.4, we will constrain the proton contributions in the case of $B_{\mathrm{tot}} \approx B_{\mathrm{LOS}}$ in Equation (19). At the moment, this is the only case that we can deal with within this simple framework.

5.3. Plasma Composition and the $e^{\pm}/p$-coupling Rate

To further constrain physical properties at the jet base, here we introduce the basic plasma properties and define general notations. The number densities of protons (n_p), positrons (n_+), and electrons (n_-) are defined as follows, respectively:

$$\begin{aligned} & n_p \equiv \eta n_-, \\ & n_+ = (1-\eta)n_- \quad (0\leqslant\eta\leqslant 1), \\ & n_p = n_{e^-p} \approx \frac{\eta}{2-\eta}\frac{1}{p-1}K_{\pm}\gamma_{\pm,\mathrm{min}}^{-p+1}, \end{aligned} \tag{21}$$

where η is a free parameter describing the proton-loading in the jet. Here we use the charge neutrality condition in the jet. It is convenient to define further quantities:

$$\begin{aligned} n_{\pm} &\equiv n_- + n_+ = (2-\eta)n_-, \\ n_{e^-p} &\equiv \eta n_- = n_p, \end{aligned} \tag{22}$$

where $n_{\pm}$ and n_{e^-p} are the number density of the electrons and positrons and that of the proton-associated electrons, respectively. The case of $\eta = 0$ corresponds to pure $e^{\pm}$ plasma, whereas $\eta = 1$ corresponds to the pure e^-/p plasma. Next, it is important to clarify the energy balances between the electrons and protons. It is useful to introduce the parameter ζ defining the average energy ratio between the protons and electrons as

$$\epsilon_{\pm} \equiv \zeta\epsilon_p, \quad \left(\frac{m_e}{m_p}\leqslant\zeta\leqslant 1\right), \tag{23}$$

where $\epsilon_{\pm}$ is the average energy of the relativistic $e^{\pm}$. The case $\zeta = 1$ can be realized for equipartition between the electrons, positrons, and protons via effective $e^{\pm}/p$ coupling, whereas $\zeta = m_e/m_p$ means inefficient $e^{\pm}/p$ coupling, for example, through randomization of bulk kinetic energy of the jet flow (e.g., Kino et al. 2012 and reference therein). Because we focus on the case of $p > 2$ suggested in M87 (Doi et al. 2013), relativistic electrons at minimum Lorentz factors characterize the total energetics. Here, $\epsilon_{\pm} \approx \gamma_{\pm,\mathrm{min}} m_e c^2$ can be estimated as $0.5\,\mathrm{MeV}\leqslant\epsilon_{\pm}\leqslant 50\,\mathrm{MeV}$ together with $1\leqslant\gamma_{\pm,\mathrm{min}}\leqslant 100$ based on the obtained $\gamma_{\pm,\mathrm{min}}$. Then, the case $\zeta = 1$ corresponds to that of nonrelativistic protons ($0.5\,\mathrm{MeV}\leqslant\epsilon_p\leqslant 50\,\mathrm{MeV}$), whereas the case $\zeta = m_e/m_p$ coincides with that of relativistic protons ($1\,\mathrm{GeV}\leqslant\epsilon_p\leqslant 100\,\mathrm{GeV}$).

In general, L is decomposed to

$$\begin{aligned} L_{\mathrm{jet}} &= L_{\pm} + L_p + L_{\mathrm{poy}}, \\ L_{\pm} &\equiv L_- + L_+, \end{aligned} \tag{24}$$

where $L_{\pm}$, L_-, L_+, L_p, and L_{poy} are, the powers of the sum of the electrons and positrons, electrons, positrons, protons, and magnetic fields. respectively. For convenience, we define η_{eq} for $L_p = L_{\pm}$, and it is given by

$$\begin{aligned} & \eta_{\mathrm{eq}} \equiv \frac{2\zeta}{1+\zeta}, \\ & L_p > L_{\pm} \quad \text{for} \quad \eta > \eta_{\mathrm{eq}}, \\ & L_p = L_{\pm} \quad \text{for} \quad \eta = \eta_{\mathrm{eq}}, \text{ and} \\ & L_p < L_{\pm} \quad \text{for} \quad \eta < \eta_{\mathrm{eq}}. \end{aligned} \tag{25}$$

Because we set

$$U_{\pm} \approx \epsilon_{\pm} n_{\pm}, \tag{26}$$

$$U_p \approx \epsilon_p n_p = \epsilon_p n_{e^-p}, \tag{27}$$

$L_p/L_{\pm} = U_p/U_{\pm} = \eta/[(2-\eta)\zeta]$ holds. Finally, the time-averaged total power of the jet (L_{jet}) can be generalized as follows:

$$L_{\mathrm{jet}} \geqslant \max\left[L_{\mathrm{poy}}, \left(1+\frac{\eta}{2-\eta}\frac{1}{\zeta}\right)L_{\pm}\right]. \tag{28}$$

Given the two model parameters, η and ζ, we obtain U_p.

5.4. Limits on B_{tot}, θ_{thick}, $U_{\pm}/U_B$, and U_p/U_B

Here, we give limits on B_{tot}, θ_{thick}, $U_{\pm}/U_B$, and U_p/U_B in the EHT region for $e^-/e^+/p$mixed plasma. As for the plasma properties, the following four cases with proton-loaded plasma can be considered, i.e., relativistic protons with e^-/p-dominated

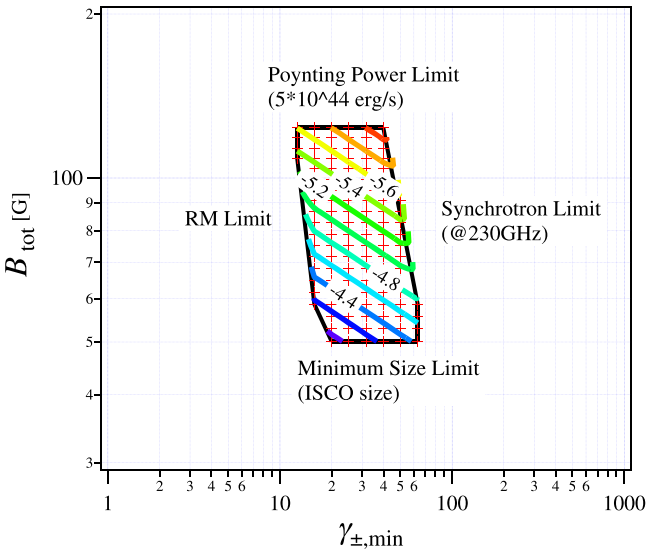

Figure 4. Allowed region of $\gamma_{\pm,\rm min}$ and $B_{\rm tot}$ when the RM limit is taken into account. The physical quantities and parameters adopted are $L_{\rm jet} = 5 \times 10^{44}\,{\rm erg\,s^{-1}}$, $p = 3.0$, $\eta = 0.99$, and $\zeta = m_e/m_p$, which corresponds to the e^-/p-dominated composition with relativistic protons. The tags $\log(U_\pm/U_B) = -4.4$, -4.8, -5.2, -5.4, and -5.6 are marked as reference values.

composition, relativistic protons with $e^\pm$-dominated composition, nonrelativistic protons with e^-/p-dominated composition, and nonrelativistic protons with $e^\pm$-dominated composition.

5.4.1. Case for Relativistic Protons ($\zeta = m_e/m_p$)

Here we consider the case for relativistic protons ($\zeta = m_e/m_p$). In Figure 4, we show a typical example of the "e^-/p-dominated" case with $\eta = 0.99$. In this case, we obtain $\eta_{\rm eq} = 1.09 \times 10^{-3}$. Because we consider the "e^-/p-dominated" composition, the upper limit of RM significantly constrains smaller $\gamma_{\pm,\rm min}$, according to Equation (19). In this case, $U_B \gg U_\pm$ still holds, as the smaller $\gamma_{\pm,\rm min}$ region is excluded by the RM constraint. In Table 2, we summarize the resultant allowed physical quantities in this case. The maximum value of $B_{\rm tot}$ is determined by the condition $L_{\rm poy} \leqslant L_{\rm jet}$, whereas the minimum value of $B_{\rm tot}$ is governed by the condition that $\theta_{\rm thick} \geqslant R_{\rm ISCO}/D_L \approx 21\,\mu$as. In the limit of inefficient $e^\pm/p$ coupling, the minimum energies of the electrons/positrons are smaller than that of the protons by a factor of m_e/m_p (i.e., $\epsilon_{\pm,\rm min} = (m_e/m_p)\epsilon_{p,\rm min}$). Therefore, $L_\pm$ decreases, and L_p tends to dominate over $L_\pm$. The energetics constraint in this case is given by $L_{\rm jet} \geqslant \max\left[L_{\rm poy}, \left(1 + \frac{\eta}{2-\eta}\frac{m_p}{m_e}\right)L_\pm\right]$.

In the case of the $e^\pm$-dominated composition with smaller η also leads to the same $B_{\rm tot}$ and $U_\pm/U_B$. In the same way as shown above, the maximum and minimum values of $B_{\rm tot}$ are determined by the jet power limit and minimum size limit at the EHT region. However, U_p is much smaller than U_B, simply because of the paucity of the relativistic proton component.

5.4.2. Cases for Nonrelativistic Protons ($\zeta = 1$)

Next, let us consider the case of nonrelativistic protons ($\zeta = 1$). When nonrelativistic protons are loaded, the corresponding energetic condition can be given by $L_{\rm jet} \geqslant \max\left[L_{\rm poy}, \left(1 + \frac{\eta}{2-\eta}\right)L_\pm\right]$. Because the protons are nonrelativistic, the effect of proton-loading is quite small in terms of energetics. The coefficient resides in a narrow range, $1 < (1 + \eta/(2-\eta)) < 3/2$. Note that RM strongly depends on η, whereas RM is independent of ζ.

The "e^-/p-dominated" case results in similar values of $B_{\rm tot}$ and $U_\pm/U_B$ to those shown in Table 2 because the maximum and minimum values of $B_{\rm tot}$ are also determined by the jet power limit and minimum size limit at the EHT region. The contributions of the protons are only $U_p = U_\pm/2$. So, this does not give any significant effects on energetics.

Finally, we comment on the "$e^\pm$-dominated" case. The main difference between the "e^-/p-dominated" and "$e^\pm$-dominated" cases is n_{e^-p}. Because the number density of the $e^\pm$-pairs does not contribute to RM, the constraint of RM becomes weaker when n_{e^-p} becomes smaller. It leads to a wider allowed region for smaller $\gamma_\pm$ and a smaller B region. Therefore, the maximum value of the allowed $U_\pm/U_B$ for the "$e^\pm$-dominated" case becomes larger than that for the "e^-/p-dominated" case. However, this only changes the allowed $\gamma_\pm$ within a factor of $\sim$10, and it does not give a large impact on energetics.

6. FULLY SSA-THIN CASE

It is worthwhile to examine a case of a fully SSA-thin model for the EHT region because the indication of $\nu_{\rm ssa} > 100$ GHz by interferometry observations does not necessarily mean that $\nu_{\rm ssa}$ is larger than 230 GHz. We can safely regard the SSA frequency as 43 GHz $< \nu_{\rm ssa} <$ 230 GHz where the lower limit is warranted by the detection of the core-shift at 43 GHz in Hada et al. (2011).

In Figure 5, we show a schematic draw of the synchrotron spectrum when the EHT region is SSA-thin at 230 GHz (solid line). The upper limit of the flux density at 43 GHz of the 230 GHz core is estimated as 0.09 Jy = 0.7 Jy $\times$ $(40/110)^2$ based on the Very Long Baseline Array (VLBA) measurements of the radio core flux and size given by Hada et al. (2013). The gray-colored scale shows the typical flux density obtained by SMA and CARMA. Interferometric observation shows some variability at 230 GHz (Akiyama et al. 2014). We define this as $F_{\rm upper}$, and we assume that $F_{\rm upper}$ is the upper limit of the flux density in the overall frequency range of 43 GHz $< \nu_{\rm ssa} <$ 230 GHz. First, from the EHT data, we can estimate a possible lower limit of $\nu_{\rm ssa}$ as

$$\nu_{\rm ssa} \geqslant 230\ {\rm GHz} \times \left(\frac{F_{\rm upper}/2.3\ {\rm Jy}}{S_\nu/1\ {\rm Jy}}\right)^{-1/\alpha} \sim 160\ {\rm GHz\ (for}\ \alpha = 2.5). \quad (29)$$

Note that the choice of $\alpha = 3.0$ leads to $\nu_{\rm ssa} \sim 170$ GHz. Second, from the VLBA data, we can estimate a possible upper limit of $\nu_{\rm ssa}$ as

$$\nu_{\rm ssa} \leqslant 43\ {\rm GHz} \times \left(\frac{F_{\rm upper}/2.3\ {\rm Jy}}{S_\nu/0.09\ {\rm Jy}}\right)^{2/5} \sim 160\ {\rm GHz}. \quad (30)$$

Table 2
Results for the Case of the e^-/p-dominated Composition with Relativistic Protons

η	Allowed $B_{\rm tot}$ (G)	Allowed $\theta_{\rm thick}$ (μas)	Allowed $U_\pm/U_B$	Allowed U_p/U_B
0.9	$50 \leqslant B_{\rm tot} \leqslant 124$	$21 \leqslant \theta_{\rm thick} \leqslant 26.3$	$7.9 \times 10^{-7} \leqslant \frac{U_\pm}{U_B} \leqslant 1.1 \times 10^{-4}$	$1.2 \times 10^{-3} \leqslant \frac{U_p}{U_B} \leqslant 0.17$
0.99	$50 \leqslant B_{\rm tot} \leqslant 124$	$21 \leqslant \theta_{\rm thick} \leqslant 26.3$	$7.9 \times 10^{-7} \leqslant \frac{U_\pm}{U_B} \leqslant 1.1 \times 10^{-4}$	$1.4 \times 10^{-3} \leqslant \frac{U_p}{U_B} \leqslant 0.20$
1	$50 \leqslant B_{\rm tot} \leqslant 124$	$21 \leqslant \theta_{\rm thick} \leqslant 26.3$	$7.9 \times 10^{-7} \leqslant \frac{U_\pm}{U_B} \leqslant 1.1 \times 10^{-4}$	$1.4 \times 10^{-3} \leqslant \frac{U_p}{U_B} \leqslant 0.21$

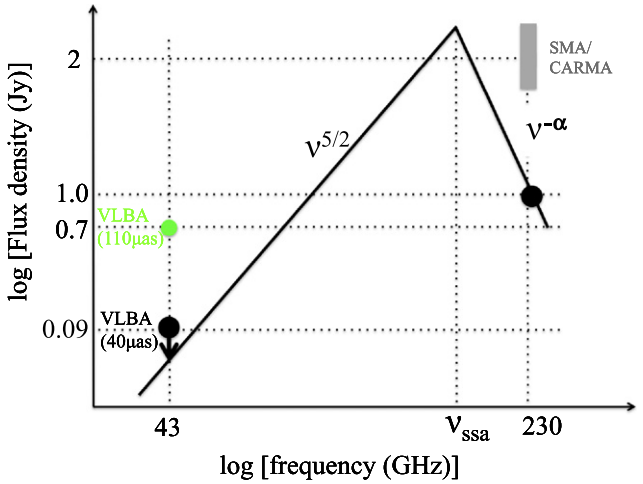

Figure 5. Schematic view of the synchrotron spectrum when the EHT region is fully SSA-thin at 230 GHz with its size and flux density, 40 μas, and 1.0 Jy (solid line). The upper limit on the flux density at 43 GHz is estimated as 0.09 Jy = 0.7 Jy $\times$ $(40/110)^2$ based on the VLBA measurements of core size and flux at 43 GHz by Hada et al. (2013). The gray-colored range shows the typical flux density at 230 GHz obtained by SMA and CARMA (e.g., Doeleman et al. 2012; Akiyama et al. 2014; Kuo et al. 2014).

Allowing some flux measurement errors, somehow we can have a consistent case around $\nu_{\rm ssa} \sim 160$ GHz with $\alpha \sim 2.5$.

Then, let us discuss the physical quantities in this case. From Equation (5), $U_\pm/U_B \propto \nu_{\rm ssa}^{-2p-13}$. Therefore, in this case, the ratio would be typically larger by a factor of $(160/230)^{-18} \sim 6.9 \times 10^2$ (for $p = 2.5$) than that for the SSA-thick case. However, this does not change the result of $U_\pm \ll U_B$ because $U_\pm \ll U_B < 10^{-4}$ in any cases with the SSA-thick core existing. Hence, we can conclude that even for the fully SSA-thin EHT region case, $U_\pm \ll U_B$ holds in order not to overproduce fluxes between 43 GHz $< \nu_{\rm ssa} <$ 230 GHz.

However, a critical difference appears for the comparison between U_p and U_B. In the case of relativistic protons with " e^-/p-dominated composition, $U_p > U_B$ can be realized for a certain range of $\nu_{\rm ssa}$. From Table 2 we know the values of U_p/U_B when $\nu_{\rm ssa} = 230$ GHz, by multiplying the factor of $\sim$200 – 400, and the maximum value reaches $U_p/U_B > 1$ at $\nu_{\rm ssa} \sim 160$ GHz.

7. SUMMARY

We have explored the magnetization degree of the jet base of M87 based on the observational data of the EHT obtained by Doeleman et al. (2012). Following the method in K14, we estimate the energy densities of the magnetic fields (U_B) and electrons and positrons ($U_\pm$) in the region detected by EHT (the EHT region) with its FWHM size, 40 μas. Imposing the basic energetics of the M87 jet, the constraints from the EHT observational data, and the minimum size of the SSA-thick region as the ISCO radius, we find the following.

1. First, we adopt the assumption that the EHT region contains an SSA-thick region. Then, the coexistence of the SSA-thick and SSA-thin regions is required for the EHT region not to overproduce $L_{\rm poy}$. The angular size of the SSA-thick region is limited as 21 μas $\leqslant \theta_{\rm thick} \leqslant$ 25.5 μas, whereas that of the SSA-thin region should be 40 μas to explain the EHT data. The derived flux density of the SSA-thick region is about 0.27 Jy. The allowed magnetic-field strength in the SSA-thick region is 58 G $\leqslant B_{\rm tot} \leqslant$ 127 G. In terms of the energetics, $U_B \gg U_\pm$ is realized at the overall SSA-thick region. If protons do not dominantly contribute to the jet energetics, then this result supports the magnetic-driven jet scenario at the SSA-thick region. We further examine the following four cases for the electron/positron/proton ($e^-/e^+/p$) mixed plasma; nonrelativistic protons with e^-/p-dominated composition, nonrelativistic protons with $e^\pm$-dominated composition, relativistic protons with e^-/p -dominated composition, and relativistic protons with $e^\pm$ -dominated composition, together with the assumption that RM detected by SMA (Kuo et al. 2014) gives an upper limit of RM of the EHT region. Although the RM limit can give tighter constraints on allowed $\gamma_\pm$, it does not change the results significantly. We find that $U_B \gg U_\pm$ always holds in any case.
2. Second, the case of the completely SSA-thin ($\nu_{\rm ssa} <$ 230 GHz) EHT region is also discussed. Although lower $\nu_{\rm ssa}$ can increase the ratio $U_\pm/U_B$ by a factor of 200–400 than that for the SSA-thick case, this does not change the result of $U_\pm \ll U_B$ because $U_\pm/U_B < 10^{-3}$. However, we also find that in the case of relativistic protons with "e^-/p-dominated" composition, $U_p > U_B$ can be realized around $\nu_{\rm ssa} \sim 160$ GHz. Future work and key questions are enumerated below.

1. An important future work is to confirm the existence of the SSA-thick region in the EHT region. If we confirm it, then we can exclude the case of $U_p/U_B > 1$. In the context of confirming the existence of the SSA-thick region, we also note the effectiveness of inclusions of longer baselines, even for a single-frequency VLBI observation. In Figure 2, it is clear that the visibility amplitude of the SSA-thin component is much smaller than that of the SSA-thick component above $\sim 3G\lambda$ at the 1.3 mm wavelength. Therefore, inclusions of baselines with $>3G\lambda$ would be effective to distinguish the SSA-thick component. For example, phased ALMA plus SMT with an effective bandwidth of 4 GHz would be effective

at $\sim$5Gλ (Figure 6 in Fish et al. 2013). In Figure 2, we show the corresponding baseline-length range (the blue-shaded region).

2. Equally important future work is to observe the EHT region with the spatial resolution of $\sim 1\,R_s$ of M87. Currently, the EHT array with 20–30 μas resolution at 230 and 345 GHz (e.g., Lu et al. 2014) is not able to reach $\sim 1\,R_s$ of M87. Ground-based short-millimeter VLBI observations are very sensitive to weather conditions (e.g., Thompson et al. 2001). To confirm our assumption that the minimum $\theta_{\rm thick} D_L$ is comparable to $\sim R_{\rm ISCO}$ or even smaller, space VLBI observations would be required in the future. In the past missions and existing plan of space VLBI, it was not possible to reach the event horizon scale of M87 (e.g., Dodson et al. 2006; Asada et al. 2009; Takahashi & Mineshige 2011; Dodson et al. 2013) because the target wavelengths were not short enough. Thus, the atmospheric-free space (sub) millimeter VLBI observation would be indispensable to reach $\sim 1\,R_s$ of M87. The phased ALMA (e.g., Alef et al. 2012, Fish et al. 2013) will play a definitive role for such observations for obtaining visibilities between space and ground telescope baselines. Honma et al. (2014) have recently proposed a new technique of VLBI data analysis to obtain superresolution images with radio interferometry using sparse modeling. The usage of the sparse modeling enables us to obtain superresolution images in which structure finer than the standard beam size can be recognized. A test simulation for imaging of the jet base of M87 is actually demonstrated in Honma et al. (2014), and the technique works well. Therefore, this superresolution technique will become another important tool for obtaining better resolution images.
3. The observational result of Doeleman et al. (2012) does not show flux variability at 230 GHz. However, the total epoch number of EHT observations is too scarce to confirm the absence of flux variability at 230 GHz all of the time. M87 might be in a quiescent state during the EHT observations in 2010 April by chance. We also emphasize that the derived field strength is still $\geqslant$58 G, and $t_{\pm,\rm syn}$ still tends to be smaller than the day scale. It is also intriguing that the same correlated flux densities in 2009 reported by Doeleman et al. (2012) are observed during another EHT observation performed in 2012 April (Akiyama et al. 2014). This result is quite different from the day-scale variability detected in Sagittarius A^* by the EHT observations (Fish et al. 2011). To search for a possible flux variability of M87 in more detail, continuous monitoring by EHT would be essential.
4. Based on the GRMHD model, well-ordered poloidal fields are dominant within the Alfvén point, and toroidal fields become dominant outside of the Alfvén point, whereas turbulence may not yet develop at the jet base (e.g., Spruit 2010 for review). In general, turbulent eddies which most probably generate turbulent fields are not expected before sufficient interactions with surrounding ambient matter (e.g., Mizuta et al. 2010 and reference therein). Therefore, a higher LP degree is likely to be expected. Conservatively saying, the reason of the low LP degree by Kuo et al. (2014) is most probably because of depolarization within the SMA beam. At the moment, we are not able to rule out a possible constitution of RIAF emission, which may also lead to low LP degree. If so, then studies of fundamental process for particle accelerations in RIAF (e.g., Hoshino 2013) and the effects on particle escape from RIAF (Le & Becker 2004; Toma & Takahara 2012; Kimura et al. 2014) would become more important.
5. In terms of the brightness temperature of the 230 GHz radio core of M87, $T_b \sim 2 \times 10^{10}\,{\rm K}\left(\frac{S_\nu}{1\,{\rm Jy}}\right)\left(\frac{\theta_{\rm FWHM}}{40\,\mu{\rm as}}\right)^{-2}$ seems slightly higher than the prediction of the hot electron temperature of $\sim 10^9$ K in RIAF flows (e.g., Manmoto et al. 1997). Hence, the jet emission seems to be preferred to explain the EHT emission in M87 (Dexter et al. 2012; see Ulvestad & Ho 2001 for similar arguments). However, it is not conclusive because the geometry near the ISCO regions is highly uncertain in the observational point of view. The scrutiny of the origin of the 230 GHz emission is still a noteworthy issue to explore.
6. Further polarimetric observation would be required to examine the RM properties in more detail. Although we adopt the RM values of Kuo et al. (2014), it is found that the observed electric vector position angle trend does not show a sufficiently tight fit to the λ^2-law. This behavior may not be due to the consequence of blending of multiple cross-polarized substructures with different RM values, but simply rather due to the nonuniformity between the upper and lower side bands of the SMA. A polarimetric observation with ALMA is clearly one of the promising first steps to improve this point. Obviously, in the final stage, short-millimeter (and submillimeter) VLBI polarimetric observations are inevitable to avoid contamination from the extended region.
7. The degree of the $e^{\pm}/p$ coupling is a critical factor for the results of the proton power. Theoretically, Hoshino & Arons (1991) found the energy transfer process from protons to positrons via the absorption of high harmonic ion cyclotron waves emitted by the protons. Amato & Arons (2006) indeed performed one-dimensional particle-in-cell (PIC) simulations for $e^-/e^+/p$ mixed plasma. However, there are several simplifications in PIC simulations, such as a smaller m_p/m_e ratio, etc. More intensive investigations are awaited to clarify the degree of $e^{\pm}/p$ coupling at the base of the M87 jet.
8. We make a brief comment on the effects of the magnetic-field topology and anisotropy of e^-/e^+ in terms of the energy distribution. If the e^-/e^+ energy distribution in the EHT region is isotropic, then the synchrotron absorption coefficient investigated by GS65 is applicable, and differences of field geometry would not have an impact on field strength estimation. For example, the difference of $B_{\rm tot}$ between the cases of the isotropic field (see Equation (1)) and the ordered field ($B_\perp = B_{\rm tot}$), which, directed toward LOS, is only a factor of $\sqrt{3/2}$.

However, if the e^-/e^+ energy distribution is highly anisotropic, then the well-known synchrotron emissivity and self-absorption coefficient are not applicable. Effects of the e^-/e^+ anisotropy on synchrotron radiation are not well-studied, and it is beyond the scope of this paper. Although we do not have any observational suggestions of such anisotropy of the e^-/e^+ energy distribution, it may be a new theoretical topic to

Table A1
Relevant Coefficients for $B_\perp$ and $K_\pm$

p	$b(p)$	$b(p)$ in K14	$b(p)$ in Hirotani (2005)	$b(p)$ in Marscher (1983)	$k(p)$
2.5	4.1×10^{-5}	3.3×10^{-5}	2.36×10^{-5}	3.6×10^{-5}	9.3×10^{-3}
3.0	2.4×10^{-5}	1.9×10^{-5}	2.08×10^{-5}	3.8×10^{-5}	1.4×10^{-3}
3.5	1.5×10^{-5}	1.2×10^{-5}	1.78×10^{-5}	…	2.1×10^{-4}

be explored, if observational suggestions are found in the future.

We thank the anonymous referee for constructive comments. KH and KA are supported by the Japan Society for the Promotion of Science (JSPS) Research Fellowship Program for Young Scientists.

APPENDIX
MODIFICATION OF NUMERICAL FACTORS

In order to obtain better accuracy calculation plus some modifications of the definition of $B_\perp$ and relevant corrections, the modified numerical coefficients of $b(p)$ and $k(p)$ are presented, although the corrections are small.

In K14, the magnetic-field strengths perpendicular to the local electron motions were not averaged over the pitch angle (in Equation (1) in K14). In this work, in Equation (1), we conduct the pitch-angle averaging for defining the averaged magnetic-field strengths perpendicular to the local electron motions.

The SSA coefficient measured in the comoving frame is given by (Equations 4.18 and 4.19 in GS65; Equation 6.53 in Rybicki & Lightman 1979)

$$\alpha_\nu = \frac{\sqrt{3}\,e^3}{8\pi m_e}\left(\frac{3e}{2\pi m_e^3 c^5}\right)^{p/2} c_1(p) K_\pm B_\perp^{(p+2)/2}\nu^{-(p+4)/2}, \quad \text{(A1)}$$

where the numerical coefficient $c_1(p)$ is expressed by using the gamma functions as follows; $c_1(p) = \Gamma[(3p+2)/12]\Gamma[(3p+22)/12]$. For convenience, we define $\alpha_\nu = X_1 c_1(p) B_\perp^{(p+2)/2} K_\pm \nu^{-(p+4)/2}$.

Optically thin synchrotron emissivity per unit frequency ϵ_ν from the uniform emitting region is given by (Equations (4.59) and (4.60) in BG70; see also Equations (3.28), (3.31) and (3.32) in GS65)

$$\epsilon_\nu = 4\pi\frac{\sqrt{3}\,e^3}{8\sqrt{\pi}\,m_e c^2}\left(\frac{3e}{2\pi m_e^3 c^5}\right)^{(p-1)/2} c_2(p) K_\pm B_{\rm tot}^{(p+1)/2}\nu^{-(p-1)/2}, \quad \text{(A2)}$$

where the numerical coefficient is $c_2(p) = \Gamma[(3p+19)/12]\,\Gamma[(3p-1)/12)]\Gamma[(p+5)/4)]/\Gamma[(p+7)/4)]/(p+1)$. In K14, $B_{\rm tot}$ was wrongly written as $B_\perp$. Therefore, here we revise it, and it leads to larger $b(p)$ by the factor of $\sqrt{1.5}$. For convenience, we define $\epsilon_\nu \equiv 4\pi X_2 c_2(p) B_{\rm tot}^{(p+1)/2} K_\pm \nu^{-(p-1)/2}$. The modified coefficient $b(p)$ is expressed as

$$b(p) = \left(\frac{4\pi c_2 X_2 \times 1.5^{1/4}}{6 c_1 X_1}\right)^2 \times 2^{-4}. \quad \text{(A3)}$$

In K14, the index of the square bracket at the right-hand side of $b(k)$ should not be 2 but -2(typo). The expression of $k(p) \propto b(p)^{(-p-2)/2}$ does not change, but the value of $k(p)$ is changed. Although the modifications of b and k in Table 1 of K14 are straightforward, based on the above explanations, we provide Table A1 for convenience.

REFERENCES

Abdo, A. A., Ackermann, M., Ajello, M., et al. 2009, ApJ, 707, 55
Akiyama, K., Lu, R.-S., & Fish, V. L. 2015, ApJ, submitted
Alef, W., Anderson, J., Rottmann, H., et al. 2012, in Proc. of Science: 11th European VLBI Network Symp, P.S (11th EVN Symposium) 053
Amato, E., & Arons, J. 2006, ApJ, 653, 325
Asada, K., Nakamura, M., Doi, A., Nagai, H., & Inoue, M. 2014, ApJL, 781, L2
Asada, K., Doi, A., Kino, M., et al. 2009, Approaching Micro-Arcsecond Resolution with VSOP-2: Astrophysics and Technologies, Vol. 402
Asano, K., & Takahara, F. 2009, ApJL, 690, L81
Begelman, M. C., Blandford, R. D., & Rees, M. J. 1984, RvMP, 56, 255
Bessho, N., & Bhattacharjee, A. 2007, PhPl, 14, 056503
Bessho, N., & Bhattacharjee, A. 2012, ApJ, 750, 129
Bicknell, G. V., & Begelman, M. C. 1996, ApJ, 467, 597
Blakeslee, J. P., Jordán, A., Mei, S., et al. 2009, ApJ, 694, 556
Blandford, R. D., & Payne, D. G. 1982, MNRAS, 199, 883
Blandford, R. D., & Rees, M. J. 1978, PhyS, 17, 265
Blandford, R. D., & Znajek, R. L. 1977, MNRAS, 179, 433
Broderick, A. E., & McKinney, J. C. 2010, ApJ, 725, 750
Broderick, A. E., & Loeb, A. 2009, ApJ, 697, 1164
Burbidge, G. R., Jones, T. W., & Odell, S. L. 1974, ApJ, 193, 43
Chandrasekhar, S. 1967, An Introduction to the Study of Stellar Structure (New York: Dover)
Chiueh, T., Li, Z.-Y., & Begelman, M. C. 1991, ApJ, 377, 462
Cotton, W. D., Wittels, J. J., Shapiro, I. I., et al. 1980, ApJL, 238, L123
Despringre, V., Fraix-Burnet, D., & Davoust, E. 1996, A&A, 309, 375
Dexter, J., McKinney, J. C., & Agol, E. 2012, MNRAS, 421, 1517
Dodson, R., Rioja, M., Asaki, Y., et al. 2013, AJ, 145, 147
Dodson, R., Edwards, P. G., & Hirabayashi, H. 2006, PASJ, 58, 243
Doeleman, S. S., Fish, V. L., Schenck, D. E., et al. 2012, Sci, 338, 355
Doeleman, S. S., Fish, V. L., Broderick, A. E., Loeb, A., & Rogers, A. E. E. 2009, ApJ, 695, 59
Doi, A., Hada, K., Nagai, H., et al. 2013, in EPJ Web of Conf. 61, The Innermost Regions of Relativistic Jets and Their Magnetic Fields (Granada, Spain) ed. J. L. Gomez (Les Ulis: EDP Sciences), 8008
Falcke, H., Melia, F., & Agol, E. 2000, ApJL, 528, L13
Fish, V., Alef, W., Anderson, J., et al. 2013, arXiv:1309.3519
Fish, V. L., Doeleman, S. S., Beaudoin, C., et al. 2011, ApJL, 727, L36
Gebhardt, K., & Thomas, J. 2009, ApJ, 700, 1690
Ginzburg, V. L., & Syrovatskii, S. I. 1965, ARA&A, 3, 297
Hada, K., Giroletti, M., Kino, M., et al. 2014, ApJ, 788, 165
Hada, K., Kino, M., Doi, A., et al. 2013a, ApJ, 775, 70
Hada, K., Doi, A., Kino, M., et al. 2011, Natur, 477, 185
Hirotani, K. 2005, ApJ, 619, 73
Honma, M., Akiyama, K., Uemura, M., & Ikeda, S. 2014, PASJ, 66, 95
Hoshino, M. 2013, ApJ, 773, 118
Hoshino, M., & Arons, J. 1991, PhFlB, 3, 818
Iwamoto, S., & Takahara, F. 2002, ApJ, 565, 163
Jones, T. W., & Odell, S. L. 1977, ApJ, 214, 522
Jones, T. W., O'dell, S. L., & Stein, W. A. 1974a, ApJ, 192, 261
Jones, T. W., O'dell, S. L., & Stein, W. A. 1974b, ApJ, 188, 353
Jordán, A., Côté, P., Blakeslee, J. P., et al. 2005, ApJ, 634, 1002
Junor, W., Biretta, J. A., & Livio, M. 1999, Natur, 401, 891
Kato, S., Fukue, J., & Mineshige, S. 1998, Black-hole Accretion Disks (Kyoto: Kyoto Univ. Press)

Kellermann, K. I., & Pauliny-Toth, I. I. K. 1969, ApJL, 155, L71
Kimura, S. S., Toma, K., & Takahara, F. 2014, ApJ, 791, 100
Kino, M., Takahara, F., Hada, K., & Doi, A. 2014, ApJ, 786, 5
Kino, M., Kawakatu, N., & Takahara, F. 2012, ApJ, 751, 101
Kirk, J. G., & Skjæraasen, O. 2003, ApJ, 591, 366
Koide, S., Shibata, K., Kudoh, T., & Meier, D. L. 2002, Sci, 295, 1688
Komissarov, S. S., Vlahakis, N., Konigl, A., & Barkov, M. V. 2009, MNRAS, 394, 1182
Komissarov, S. S., Barkov, M. V., Vlahakis, N., & Konigl, A. 2007, MNRAS, 380, 51
Krichbaum, T. P., Graham, D. A., Bremer, M., et al. 2006, JPhCS, 54, 328
Krolik, J. H., Hawley, J. F., & Hirose, S. 2005, ApJ, 622, 1008
Kuo, C. Y., Asada, K., Rao, R., et al. 2014, ApJL, 783, L33
Le, T., & Becker, P. A. 2004, ApJL, 617, L25
Lee, S.-S. 2013, JKAS, 46, 243
Li, Z.-Y., Chiueh, T., & Begelman, M. C. 1992, ApJ, 394, 459
Loeb, A., & Waxman, E. 2007, JCAP, 3, 011
Lu, R.-S., Broderick, A. E., Baron, F., et al. 2014, ApJ, 788, 120
Lu, R.-S., Fish, V. L., Weintroub, J., et al. 2012, ApJL, 757, L14
Macchetto, F., Marconi, A., Axon, D. J., et al. 1997, ApJ, 489, 579
Manmoto, T., Mineshige, S., & Kusunose, M. 1997, ApJ, 489, 791
Marscher, A. P. 1987, Superluminal Radio Sources (Cambridge: Cambridge Univ. Press)
Marscher, A. P. 1983, ApJ, 264, 296
Marscher, A. P. 1977, AJ, 82, 781
McKinney, J. C., Tchekhovskoy, A., & Blandford, R. D. 2013, Sci, 339, 49
McKinney, J. C. 2006, MNRAS, 368, 1561
McKinney, J. C., & Gammie, C. F. 2004, ApJ, 611, 977
Mizuta, A., Kino, M., & Nagakura, H. 2010, ApJL, 709, L83
Nagakura, H., & Takahashi, R. 2010, ApJ, 711, 222
Nakamura, M., & Asada, K. 2013, ApJ, 775, 118
Okamoto, I. 1999, MNRAS, 307, 253
Okamoto, I. 1974, MNRAS, 167, 457
Owen, F. N., Eilek, J. A., & Kassim, N. E. 2000, ApJ, 543, 611
Owen, F. N., Porcas, R. W., Mufson, S. L., & Moffett, T. J. 1978, AJ, 83, 685
Pacholczyk, A. G. 1970, Series of Books in Astronomy and Astrophysics (San Francisco: Freeman)
Quataert, E., & Gruzinov, A. 2000, ApJ, 545, 842
Reynolds, C. S., Fabian, A. C., Celotti, A., & Rees, M. J. 1996, MNRAS, 283, 873
Rieger, F. M., & Aharonian, F. 2012, MPLA, 27, 30030
Rioja, M., & Dodson, R. 2011, AJ, 141, 114
Rybicki, G. B., & Lightman, A. P. 1979, Radiative Processes in Astrophysics (New York: Wiley-Interscience)
Sari, R., Piran, T., & Narayan, R. 1998, ApJL, 497, L17
Slysh, V. I. 1992, ApJ, 391, 453
Spruit, H. C. 2010, Lecture Notes in Physics, Vol. 794 (Berlin: Springer)
Stawarz, Ł., Aharonian, F., Kataoka, J., et al. 2006, MNRAS, 370, 981
Takahashi, R., & Mineshige, S. 2011, ApJ, 729, 86
Takahashi, R. 2004, ApJ, 611, 996
Takamoto, M., Inoue, T., & Inutsuka, S.-I. 2012, ApJ, 755, 76
Tan, J. C., Beuther, H., Walter, F., & Blackman, E. G. 2008, ApJ, 689, 775
Tchekhovskoy, A., Narayan, R., & McKinney, J. C. 2011, MNRAS, 418, L79
Thompson, A. R., Moran, J. M., & Swenson, G. W., Jr. 2001, in Interferometry and Synthesis in Radioastronomy, ed. A. Richard Thompson, J. M. Moran, & G. W. Swenson, Jr. (2nd ed.; New York: Wiley), 399
Toma, K., & Takahara, F. 2013, PTEP, 2013, 3E02
Toma, K., & Takahara, F. 2012, ApJ, 754, 148
Tomimatsu, A., & Takahashi, M. 2003, ApJ, 592, 321
Tsang, O., & Kirk, J. G. 2007, A&A, 476, 1151
Uchida, T. 1997, PhRvE, 56, 2181
Ulvestad, J. S., & Ho, L. C. 2001, ApJ, 558, 561
Vlahakis, N., & Konigl, A. 2003, ApJ, 596, 1080
Walsh, J. L., Barth, A. J., Ho, L. C., & Sarzi, M. 2013, ApJ, 770, 86
Young, A. J., Wilson, A. S., & Mundell, C. G. 2002, ApJ, 579, 560
Zavala, R. T., & Taylor, G. B. 2004, ApJ, 612, 749